Small angle neutron scattering investigation and the low frequency dielectric response of sintered ZrO_2–8 mol% Y_2O_3 ceramic compacts: the effect of pore characteristics

2004 J. Phys.: Condens. Matter 16 6229

(http://iopscience.iop.org/0953-8984/16/34/021)

INSTITUTE OF PHYSICS PUBLISHING JOURNAL OF PHYSICS: CONDENSED MATTER

J. Phys.: Condens. Matter **16** (2004) 6229–6242 PII: S0953-8984(04)75734-3

Small angle neutron scattering investigation and the low frequency dielectric response of sintered ZrO_2–8 mol% Y_2O_3 ceramic compacts: the effect of pore characteristics

D Sen[1], T Mahata[2], A K Patra[1], S Mazumder[1] and B P Sharma[2]

[1] Solid State Physics Division, Bhabha Atomic Research Centre, Trombay, Mumbai-400 085, India
[2] Powder Metallurgy Division, Bhabha Atomic Research Centre, Vashi Complex, New Mumbai-400 705, India

E-mail: debasis@apsara.barc.ernet.in

Received 3 February 2004
Published 13 August 2004
Online at stacks.iop.org/JPhysCM/16/6229
doi:10.1088/0953-8984/16/34/021

Abstract

The effect of the pore structure on the low frequency (0.01–100 kHz) dielectric response of sintered ZrO_2–8 mol% Y_2O_3 ceramic compacts has been investigated. Pore characteristics such as the pore size distribution, specific surface area and pore morphology have been estimated by means of small angle neutron scattering (SANS). It has been observed that both the real and the imaginary parts of the complex dielectric permittivity for the specimens depend not only on the porosity but also on the pore characteristics, significantly. Unlike in the normal Debye relaxation process, the imaginary part of the dielectric constant increases in the lower frequency region. The variation in the dielectric response is explained by a pore structure dependent interfacial polarization, ion hopping and conduction.

1. Introduction

The dielectric properties of ceramic materials are of immense technological as well as scientific interest [1]. One of the most important parameters for any dielectric material is its dielectric constant or dielectric permittivity, ε, which is a measure of the ability of a capacitor to store charge. In the presence of a sinusoidal electric field across a capacitor with a lossy dielectric, the permittivity can be expressed as $\varepsilon^* = \varepsilon' + \imath\varepsilon''$. ε' represents the real part of the permittivity (i.e., the dielectric constant) and ε'' is the imaginary part, which is a measure of the energy dissipation in the material. Dielectric loss is generally described in terms of the loss tangent $\tan(\delta) = \varepsilon''/\varepsilon'$. The factors which affect the dielectric constant and loss are broadly classified into two categories: intrinsic and extrinsic. Intrinsic losses are dependent on the

crystal structure and can be described in terms of the interaction of the phonon system with the alternating electric field. The field alters the equilibrium of the phonon system and the subsequent relaxation is associated with energy dissipation. A review on intrinsic losses has been published by Gurevich *et al* [2]. Intrinsic losses set a lower limit on the losses found in '*defect free*' single crystals. Extrinsic losses are due to factors such as different imperfections, e.g. porosity, impurities, grain boundaries, micro-cracks, random crystal orientations. It is evident from some of the earlier studies [3–5] that the losses in sintered polycrystalline ceramics are strongly affected by these extrinsic factors. Some of these works aimed at investigating the effect of impurity, total porosity and grain size on the dielectric behaviour in ceramics in the microwave region. However, it is worth mentioning that the differentiation of grain characteristics and the pore characteristics as regards the dependence of the dielectric behaviour has not been reported so far to the best of our knowledge. The contribution of the grains can be examined only in a very dense system where the contribution of the pores remains very insignificant. Interestingly, some of the previous work leads to quite different observations. One of the previous studies [3] showed no variation of the dielectric constant with grain size at very high frequency, although the dielectric loss was observed to be greater for coarser-grained alumina. In contrast to this observation, it was noted in [6] that a fine-grained ceramic showed a higher loss than ceramics with coarser-grained microstructure. The study by Iddles *et al* [7] on zirconium tin titanate ceramic showed that the grain size did not affect the loss tangent.

When a relaxation process is present, the dielectric response of materials usually shows a peak in the frequency dependence of the imaginary part of the loss component. The relaxation process may be of Debye [8] or non-Debye type [8]. If the dielectric material is a heterogeneous one, then the dielectric constant depends on the different phases present and the way in which the phases are spatially distributed. If the volume fraction of the second phase is small enough, the dielectric permittivity can be expressed [9] in terms of the permittivities and volume fractions of the individual mixture components. The frequency response is mostly of non-Debye type. However, when the volume fraction of the second phase (e.g. pores or inclusions) is significant enough, as in the case of most practical systems, then the dielectric response depends on the morphological characteristics of the heterogeneities in addition to the volume fraction. The frequency response in these cases is generally expressed using some empirical formula [8]. However, sometimes the frequency response is explained [10] by considering several relaxation terms. Although some computer models show [11] the effect of the signature of the low frequency dispersions in binary mixtures, a theoretical model for dielectric response in such heterogeneous systems with a significant volume fraction of the second phase will be of immense importance. Investigations on the effect of pore characteristics such as the pore size distribution and specific surface area on the low frequency dielectric response will contribute a great deal towards the aforementioned theoretical model and the present investigation is a step in that direction.

Small angle neutron scattering (SANS) investigation is an important and non-destructive technique for addressing the pore morphology in ceramics and other porous materials [12–15]. Zirconia (ZrO_2) based ceramics have attracted a great deal of attention because of their various technological applications. In particular, yttria-stabilized zirconia is a ceramic system with potential for use in various structural and functional applications. The ZrO_2–8 mol% Y_2O_3 composition has fluorite-type crystal structure. Oxygen vacancies are introduced in the lattice because of the aliovalent doping. Dielectric loss is expected due to ion migrations. Some earlier work dealt with small angle scattering and the microstructure in zirconia based ceramics [16–19].

The present paper deals with SANS investigation of pore characteristics and their effect on the low frequency (0.01–100 kHz) dielectric response of sintered ZrO_2–8 mol% Y_2O_3 ceramic

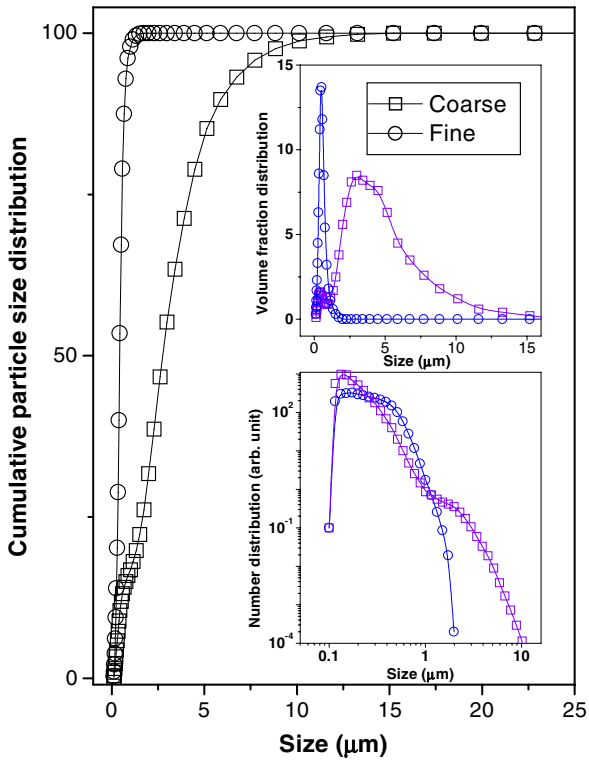

Figure 1. The initial powder particle size distribution as obtained from a laser light scattering method. The top inset shows the volume fraction distribution and the bottom inset shows the number distribution. The differences between the distributions of the PF and PC are evident.

(This figure is in colour only in the electronic version)

compacts. Experiments have been performed at two different porosity levels by varying the sintering conditions. In the present investigation we also intend to investigate the effect of pore size and pore morphology attaining a constant porosity value at two porosity levels while the pore size differs.

2. Experimental details

2.1. Sample

The preparation of yttria-stabilized zirconia (fully cubic phase) through the citric acid gel route has been described elsewhere [14]. For the present study, the gel has been calcined at two different temperatures, i.e. 800 and 950 °C. The powder calcined at 800 °C has been ball milled for 20 h to get finer powder of median particle size 0.43 μm. The 950 °C calcined powder has been hand ground in a pestle and mortar to obtain powder of median size 2.74 μm. Figure 1 represents the particle size distribution as obtained by a laser scattering particle size analyser (Horiba, LA-500). Green pellets (12 mm diameter $\times$ 3 mm thick, approximately) prepared by uniaxial pressing (200 MPa) were sintered at 1200 and 1400 °C with different soaking times (0, 1 and 3 h). The heating rate was maintained at 600 °C h^{-1} up to the final temperature. The density of the sintered pellets was determined from physical measurements. The densities

Table 1. Densities of the sintered specimens for different sintering conditions and initial particle sizes.

Temperature (°C) (Soaking time) (h)	1200 (0)	1200 (1)	1200 (3)	1400 (0)	1400 (1)	1400 (3)
Density, %TD PC	53	56	58	62	68	72
Density, %TD PF	61	73	81	89	94	96

of the sintered pellets have been tabulated in table 1. Pellets obtained from finer and coarser powders are designated as PF and PC, respectively. It is seen that the pellets PF-1200 (1 h) and PC-1400 (3 h) have almost equal porosity values ($\phi = 0.28$). Similarly, pellets PF-1200 (0 h) and PC-1400 (0 h) have porosity values that are nearly the same ($\phi = 0.39$). However, the pore connectivities are likely to be very different from each other because of the differences between the starting powders and other sintering conditions. The above two pairs of specimens have been picked for the SANS investigations for determining the pore characteristics.

2.2. SANS

SANS experiments have been performed using a double-crystal based small angle neutron scattering instrument at the Guide Tube Laboratory of Dhruva reactor at Trombay, India [20]. The instrument consists of a non-dispersive $(1, -1)$ setting of 111 reflections from silicon single crystals with the specimen between the two crystals. The scattered intensities have been recorded as a function of the wavevector transfer q ($=4\pi \sin(\theta)/\lambda$, where 2θ is the scattering angle and λ (=0.312 nm) is the incident neutron wavelength for the present experiment). The specimens under SANS investigation were placed on a sample holder with a circular slit of 1 cm diameter. In order to correct for the multiple-scattering effects [21–23] for the above specimens, SANS experiments were performed for two different thicknesses of each specimen. The measured SANS profiles have been corrected for background, transmission and instrument resolution [24]. Figures 2 and 3 depict the corrected SANS curves for the specimens. The solid line in the higher q region is a guide to the eye, to emphasize the linearity of the data on a double-logarithmic scale. Unlike in one of the earlier investigations [12], in the present case no power law behaviour [12] has been observed in the lower q region. This is indicative of the non-agglomerated nature of the powder particles and is largely achieved by the use of the proper long time ball-milling procedure, which helps to break the agglomerates.

2.3. Dielectric measurements

Capacitance and $\tan(\delta)$ values have been measured using a GenRad RLC bridge in the frequency range 0.01–100 kHz. Values of the relative permittivity (ε'_r) at various frequencies have been calculated from the measured capacitance values by using the appropriate geometric factor [8]. ε'' has been calculated by multiplying ε'_r with $\tan(\delta)$ [8]. The ε'_r and ε'' values for the specimens with $\phi = 0.28$ and 0.39 are plotted in figures 4 and 5 respectively.

3. Data analysis and discussion

Small angle neutron scattering arises from the fluctuations of the scattering length density in a specimen and the SANS profile maps the size and shape of the scattering density of

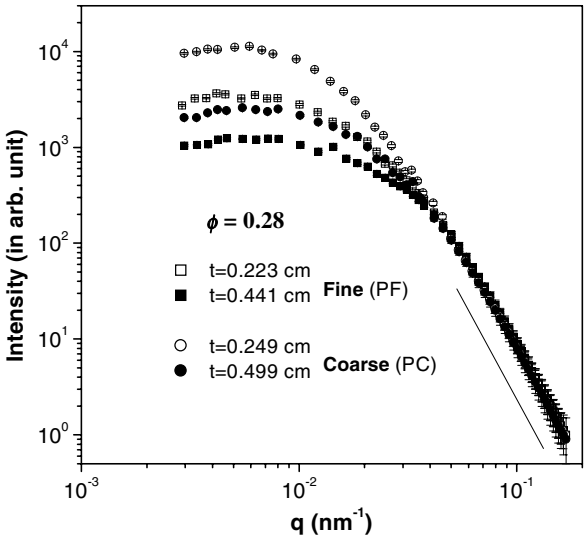

Figure 2. SANS profiles (after transmission, background and resolution correction) of the PF and PC specimens with $\phi = 0.28$ on a double-logarithmic scale. Experiments have been performed for two thicknesses of each specimen. The solid line at the tail is a guide to the eye only. The error bars are shown on the data. The error on the data at the lowest accessible q value is $\sim$1.8% and is less than the symbol size.

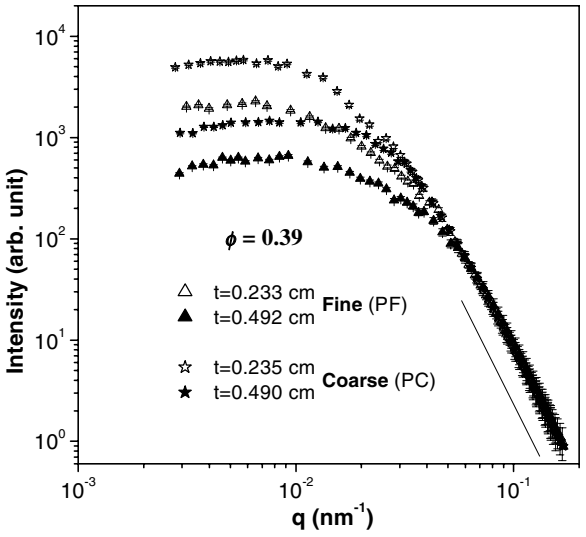

Figure 3. SANS profiles (after transmission, background and resolution correction) of the PF and PC specimens with $\phi = 0.39$ on a double-logarithmic scale. Experiments have been performed for two thicknesses of each specimen. The solid line at the tail is a guide to the eye only. The error bars are shown on the data. The error on the data at the lowest accessible q value is $\sim$1.8% and is less than the symbol size.

inhomogeneities (e.g. pores in a porous medium) in the material. In the present case, as the porosity is much less than 50%, the SANS signal is predominantly due to the pores. From figures 2 and 3, it is discernible that the sharpness of the SANS curves for the specimens with

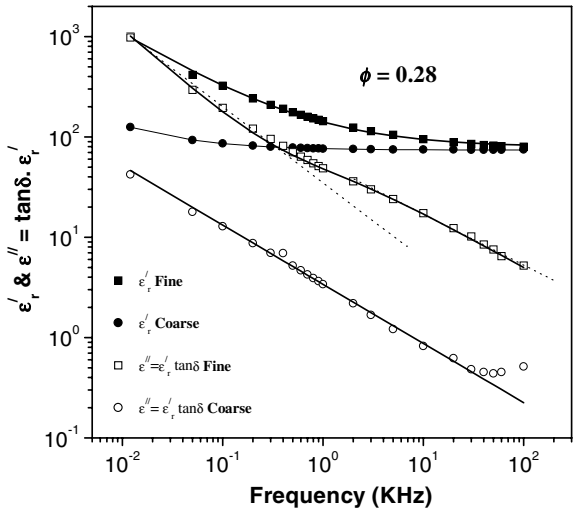

Figure 4. The frequency response of the real (ε') and imaginary (ε'') parts of the dielectric constant for the PF and PC specimens with $\phi = 0.28$. It is seen that ε'' increases with decrease in the frequency and no prominent loss peak is observed.

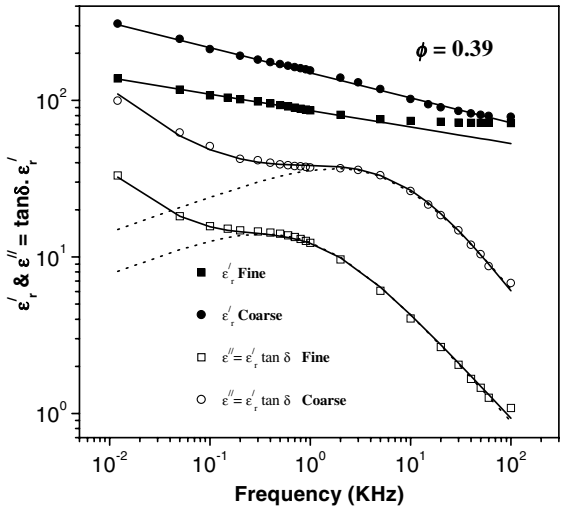

Figure 5. The frequency response of the real (ε') and imaginary (ε'') parts of the dielectric constant for the PF and PC specimens with $\phi = 0.39$. It is seen that ε'' shows a broad hump at 1–10 kHz and increases in the low frequency region.

almost identical porosity levels (of porosity 0.28 and 0.39 respectively) differ significantly for PF and PC specimens. In both cases, the curves are sharper for the PC specimens. The trend is same for both thin and thick specimens. This feature of the curves indicates, at least qualitatively at this stage, the existence of larger pores in the PC specimens. However, detailed analysis of these data will give the distribution of the pore sizes. It is interesting to see that in both cases the sharpness of the curves varies with the specimen thickness although the shape of the curves in the tail region remains unaffected. This is due to the effect of the multiple scattering [21–23] in the specimens.

Generally the SANS curves are analysed on the basis of the single-scattering approximation [21], where the neutrons passing through a specimen are either scattered only once from a single particle or not at all. However, this approximation is valid only when the specimen thickness $t \leqslant 0.1l$ (l is the scattering mean free path of the neutrons in the medium). Strongly scattering systems such as ceramics cannot always be analysed invoking the single-scattering approximation, as the specimens needed to replicate the essential properties of

the bulk matrix are thick enough to deviate from this approximation. However, it is worth mentioning that the beam-broadening feature of multiple scattering if utilized properly can be seen as a boon in a moderate resolution instrument for getting information on larger inhomogeneities, which are otherwise not accessible with such an instrument. In a multiple-scattering process the neutrons are scattered many times in single-scattering events before leaving the specimen. The effect of multiple scattering appears due to one or more of the various factors such as strong scattering contrast, long wavelength of the probing radiation, large size of the inhomogeneities and significant specimen thickness. The signature of multiple scattering [22, 23] is the broadening of the SANS curve with increase in the specimen thickness or the wavelength of the probing neutrons. The multiple scattering is generally quantified by the average number of scattering interactions (N) [21], which is the ratio of the sample thickness, t, to the mean free path, l, of the probing radiation. The single-scattering profile can be extracted from the recorded profiles, at least for the specimens of two different thickness or for two different wavelengths of the probing neutrons [21]. The algorithm for the inversion of the multiple-scattering profile is based on the principle that although the different multiple-scattering profiles are functionally distinct for different values of N, the single-scattering profiles computed from each of them are the same or least deviated provided that the correct N value is used for the inversion [21]. The most important step of this algorithm is the estimation of N for each measurement from the two computed $g_j(r)$ ($j = 1, 2$) functions in real space obtained by Hankel transformation [25, 26] ($g(r) = \int q I(q) J_0(qr)\,\mathrm{d}q$) of the two corrected SANS profiles $I_j(q)$. To determine l from measurements with two different thicknesses, the following function is used:

$$\sum_i \left[Y_1\left(r_i, \frac{t_1}{l}\right) - Y_2\left(r_i, \frac{t_2}{l}\right)\right]^2 \text{ is minimized with respect to } l.$$

The function $Y(r, N) = \frac{1}{N} \ln[\frac{g(r)}{g(0)}[\mathrm{e}^N - 1] + 1]$ is proportional to the Hankel transformed function of the single-scattering profile.

A model calculation has been performed to elaborate on this. A single-scattering profile is generated for an ensemble of polydisperse spherical pores assuming log-normal distribution:

$$\rho(R) = \frac{1}{\sqrt{2\pi\sigma^2 R^2}} \exp\left[-\frac{[\ln(R/R_0)]^2}{2\sigma^2}\right]$$

with R_0 and σ as adjustable parameters. For the present case, R_0 and σ were assumed to be 40 nm and 0.50, respectively. The simulated profile is shown in figure 6. The multiple-scattered curves have been generated for $N = 1.5$, 3.0 and 5.0 and are shown in the figure. From the profiles for $N = 1.5$ and 3.0, the single-scattering profile has been calculated back using the above algorithm and is shown in the figure. It is seen that the extracted SSP matches well with the original SSP.

Single-scattering profiles, for the specimens, are extracted using the above algorithm. The estimated values of the scattering mean free path (l) are tabulated in table 2. In figure 7, the extracted single-scattering profiles are compared to the corresponding SANS profiles for the thinner specimens. It is evident that the single-scattering profiles are sharper in the low q region but the shape of the power law region at higher q values remains unaffected.

Now, at the outset let us analyse the single-scattering profiles assuming a polydisperse spherical pore model. Here it should be mentioned that the pores in the specimens might not all be exactly spherical in shape; rather, they can be described as ellipsoids with modulated surfaces. However, in that case, analysing the data would be based on minimizing several nonlinear parameters and hence the problem of obtaining globally minimized parameters would remain unresolved. In the light of the polydisperse spherical pore model, the profiles are best

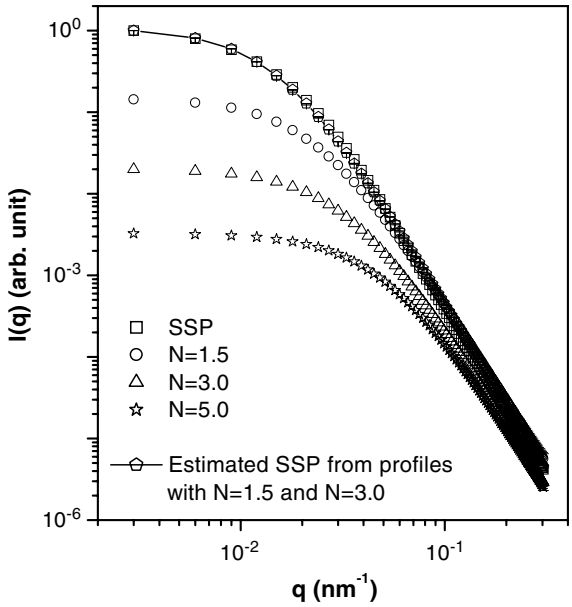

Figure 6. The results from the model calculation. The multiple-scattered profiles with $N = 1.5, 3$ and 5.0 are simulated using the model single-scattering profile which is calculated for a polydisperse ensemble of pores (mentioned in the text). The single-scattering profile is extracted back, from the profiles with $N = 1.5$ and 3.0, using the algorithm as mentioned in the text. It is seen that the extracted SSP matches well with the original model SSP. The curves for various N values are shifted vertically to compare their sharpness.

Table 2. Parameters obtained from the fit of the SANS data and the l values from the algorithm. ($\langle\,\rangle$ denotes an average value.)

Specimen	l (cm)	R_0 (nm)	σ	$\langle R\rangle$ (nm)	Specific surface area (κ) ($m^2\ m^{-3}$)
$\phi = 0.28$, fine	0.134 ± 0.016	33.83 ± 0.28	0.48 ± 0.005	37.99 ± 0.33	7.54×10^7
$\phi = 0.28$, coarse	0.103 ± 0.008	44.30 ± 0.34	0.49 ± 0.005	50.10 ± 0.39	5.58×10^7
$\phi = 0.39$, fine	0.127 ± 0.017	28.09 ± 0.26	0.48 ± 0.005	31.54 ± 0.31	9.32×10^7
$\phi = 0.39$, coarse	0.092 ± 0.008	38.99 ± 0.35	0.48 ± 0.006	43.61 ± 0.44	6.14×10^7

interpreted in terms of the radius dispersion $\rho(R)$ of the pores, in the form of a log-normal distribution. The fits of the model to the extracted SSPs are shown in figure 8. The important parameters obtained from the fit are tabulated in table 2. The estimated pore size distributions are depicted in figure 9. It is to be noted that although the above model fits the data quite well in the lower and intermediate q regions, the fit to the data in the high q region is slightly off, although it mostly lies within the error bars. This is because of the fact that in the early and in the intermediate stages of sintering the pores may not be exactly spherical in shape and the possibility of dispersion in the pore shape cannot be ruled out. From figure 9 and also from table 2, it is evident that the pore size distributions for specimens ($\phi = 0.28$ and 0.39) are different for the PF and PC specimens. The average value of the distribution for PC specimens is significantly greater than those for the PF specimens in both cases. So, it is evident that although the porosity remained nearly the same for PF and PC specimens, the

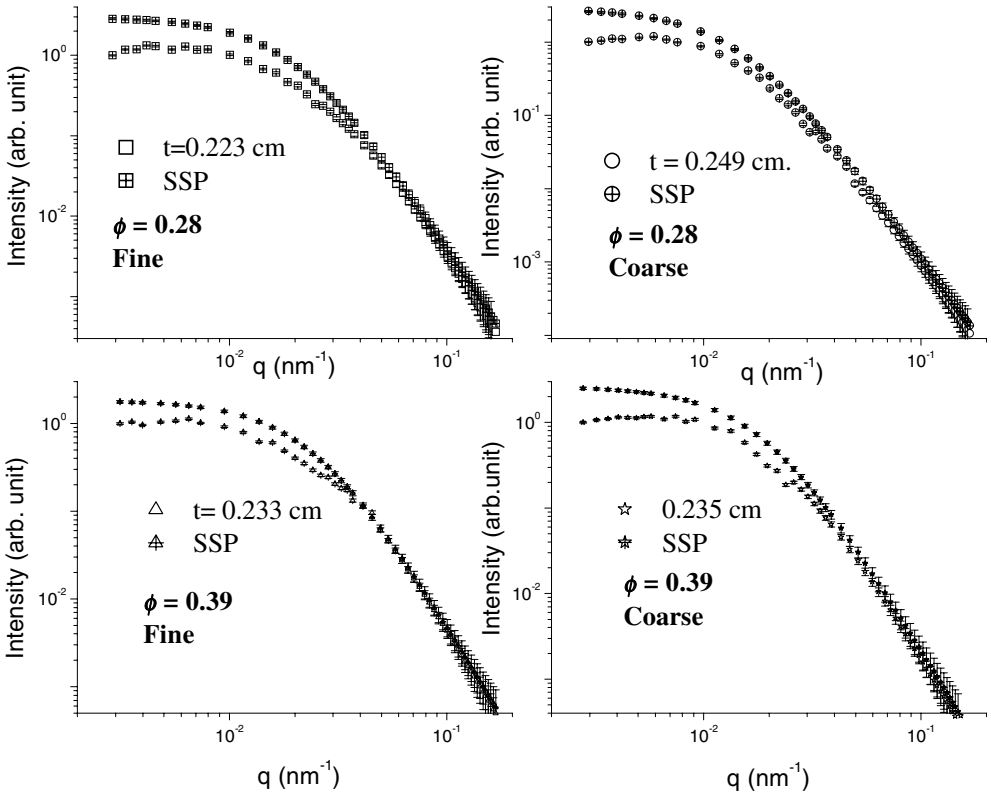

Figure 7. Extracted single-scattering profiles (SSP) are compared with the corresponding profiles for thinner specimens. The error bars are shown on the data. The error on the SSP data at the lowest accessible q value is ∼3.0% and is of the order of the symbol size.

pore size distributions and average pore radii are quite different in these specimens at both porosity levels. At this point it should also be noted that the soaking time for the specimens with $\phi = 0.39$ is negligibly small and hence it is expected that in this case the probability of interconnection between the pores is greater than that for the specimens with $\phi = 0.28$.

It is to be noted that in the SANS analysis, although the effect of multiple scattering has been taken into account, the multiple-refraction effect was neglected in the present case. The reason for neglecting the multiple-refraction effect is explained as follows. If D represents the scattering length density difference between the matrix and the pores, then the phase shift parameter (γ) is equal to $2\lambda DR$ (R being the radius of the pores). When $\gamma \gg 1$, multiple refraction has to be taken into account and $\gamma \ll 1$ for the diffraction limit. In the present case, taking $D \sim 5.05 \times 10^{-4}$ nm^{-2} for ZrO_2–8 mol% Y_2O_3 ceramic, $\lambda = 0.312$ nm and (from table 2) $\langle R \rangle \sim 50$ nm, γ is calculated to be 0.014, which is small compared to unity. This implies that the multiple-refraction effect is not significant in the present case.

As the slope of the profiles for $q > 0.05$ nm^{-1} has been found to be nearly 4.0, indicating a sharp interface, we have estimated the specific surface area (κ), the ratio of surface area to volume for the pores, from the extracted SSPs using the formula

$$\kappa = \pi \lim_{q\to\infty} \frac{[q^4 I(q)]}{\int_0^\infty I(q) q^2 \, \mathrm{d}q}.$$

The estimated κ values are tabulated in table 2. It is seen that for specimens with identical

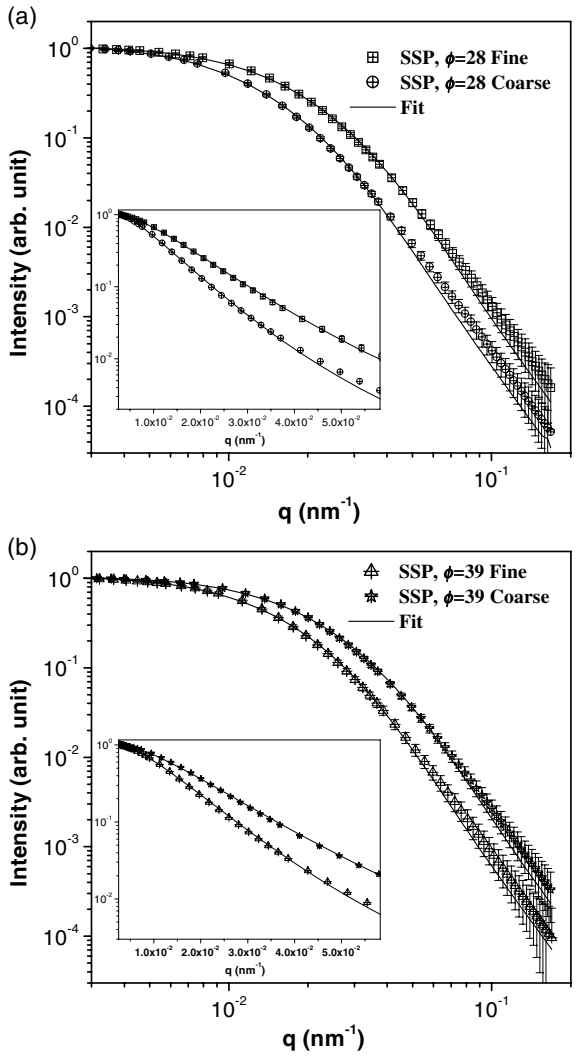

Figure 8. The fit of the polydisperse spherical pore model to the extracted single-scattering profile is shown (a) for $\phi = 0.28$ and (b) for $\phi = 0.39$. The error bars on the data are shown. The inset shows the plot on a semi-logarithmic scale.

porosity values, the κ value is greater for the PF specimens as compared to that for the PC specimens. It is important to note that the estimation of the specific surface area does not require the intensity on an absolute scale, unlike the determination of the absolute surface area.

From figures 4 and 5, showing the dielectric responses of the specimens, it is seen that at both porosity levels, ε'', unlike the normal Debye relaxation mechanism, shows an anomalous increasing trend in the low frequency region. For specimens with $\phi = 0.39$, ε'' shows a hump between 1 and 10 kHz. ε' in both cases decreases with increase in frequency and becomes almost constant in the higher frequency region. At this stage, it is worth mentioning that a porous ceramic can be regarded as a heterogeneous dielectric material where the pores are the heterogeneities. Polarization relating to complex permittivity in a dielectric medium depends on composition mixtures. Various polarization mechanisms depend differently upon the frequency. Thus the complex permittivity will differ as the frequency changes. Polarization mechanisms are generally of the form of electronic, ionic, orientational, interfacial etc. The effect of electronic and ionic polarization occurs at very high frequencies. However, ion jump

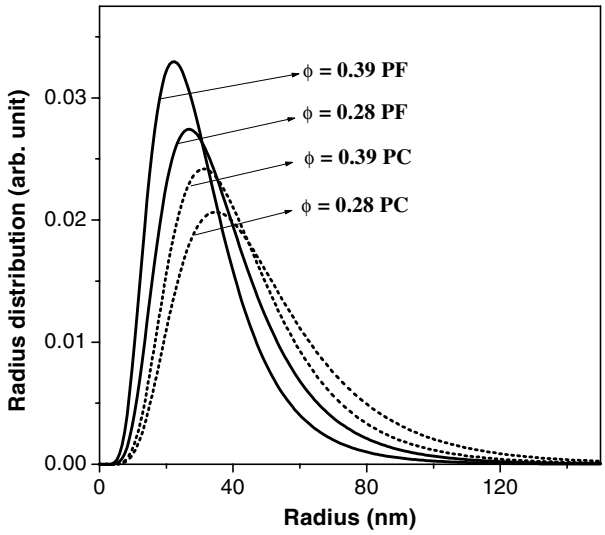

Figure 9. The estimated pore size distributions obtained from fitting the model to the SSP. It is seen that in both cases ($\phi = 0.28$ and for $\phi = 0.39$) the peak of the distribution for the PC specimen is shifted towards the higher radii side and the distributions are significantly different than those for the PF specimens.

relaxation between two equivalent ion positions is responsible for the dielectric loss factor at intermediate frequencies. Electronically heterogeneous materials experience interfacial polarization (Maxwell–Wagner effects) [27, 28] for which the effect is pronounced in the relatively low frequency region. In a heterogeneous material, the motion of the charge carriers may occur more easily through one phase and therefore be constricted at phase boundaries. As a result, charges build up at the interfaces and can be polarized in an applied field. In addition, conduction loss becomes important at very low frequencies.

In the present case, the frequency dependence of ε'' can be explained as due to the mixed contribution of ion jump and conduction losses and interfacial effects. Interfacial effects are evident from the significant variations in the response curves for PF and PC specimens, where the pore morphologies and pore sizes are different for the two specimens although the porosity remains constant. The increase in ε'' in the very low frequency region occurs mainly because of the conduction losses and Maxwell–Wagner effect. Particularly for the specimen with $\phi = 0.39$, the effect of the ion jump losses is visible as manifested by the hump at $\sim$1 kHz. However, for the specimen with $\phi = 0.28$ the effect of the conduction is more pronounced than that of the ion jump effects. This is because, for the specimen with $\phi = 0.28$, the structure is more compact and hence the probability of through migration and conduction is greater than that for the specimen with $\phi = 0.39$.

In an early work, a fractional power law behaviour of the dielectric permittivity was proposed [29]. On the basis of that, the variation of ε' with the frequency (f) could be fitted as

$$\varepsilon'_{\mathrm{r}}(f) = C_1 f^{-m} + C_2$$

where C_1 and C_2 are constants; m is the exponent of the power law.

The dielectric loss peak is represented empirically by combining two power laws; this is known as the Jonscher model [8], which is given as

Table 3. Parameters obtained from the fit of the dielectric data.

Specimen	m	m_1	n_1	f_p (kHz)	m_2
$\phi = 0.28$, fine	0.605	0.40	0.47	1.00	0.87
$\phi = 0.28$, coarse	0.680	—	—	—	0.16
$\phi = 0.39$, fine	0.10	0.40	0.30	1.00	0.60
$\phi = 0.39$, coarse	0.16	0.21	0.13	8.00	0.60

$$\varepsilon''(f) = \frac{C_3}{\left(\left(\frac{f}{f_p}\right)^{-m_1} + \left(\frac{f}{f_p}\right)^{1-n_1}\right)}$$

where f_p characterizes the peak frequency.

In our case, to fit the whole spectrum, including the low frequency anomalous increase occurring because of the conduction and interfacial effects, we added an additional term; hence the above equation becomes

$$\varepsilon''(f) = \frac{C_3}{\left(\left(\frac{f}{f_p}\right)^{-m_1} + \left(\frac{f}{f_p}\right)^{1-n_1}\right)} + C_4 f^{-m_2}.$$

The important parameters obtained from the fits are tabulated in table 3.

4. Results and discussion

From the SANS analysis, it is revealed that the pore characteristics such as the pore size distribution and specific surface area for the specimens with $\phi = 0.28$ and 0.39 are different. Even for the samples with identical porosity levels but prepared from fine and coarse powder particles (PF and PC specimens) the pore size distributions and specific surface areas differ significantly. The average value describing the pore size distribution is greater and the specific surface area is less for the PC specimens compared to the corresponding PF specimens. This indicates the lower number of pores in the PC specimens compared to the corresponding PF specimens when the porosity levels in the two cases are the same. The differences in the pore morphology, pore size, pore connectivity etc are also reflected in the low frequency dielectric response.

Careful observation of the dielectric data shows a few interesting features as follows:

(i) The anomalous increase in the low frequency behaviour of ε''.
(ii) A hump in the ε'' spectrum for the specimen with $\phi = 0.39$. The frequency (f_p) value at the hump position is eight times greater for PC specimen than for the PF specimen.
(iii) Although a significant difference arises for ε' values in the very low frequency region, they become almost identical and constant at high enough frequency for the PC and PF specimens and for both porosity levels.
(iv) ε' and ε'' are greater for the PF specimen than for the PC specimen in the case of $\phi = 0.28$. However, the trend is reversed for $\phi = 0.39$.

The anomalous behaviour of ε'' at low frequency is attributed to the loss due to ion migration, conduction and interfacial polarization mechanisms, which are strongly influenced by the morphology and the size distribution of the pores.

The hump in the ε'' spectrum for the specimens with $\phi = 0.39$ arises because of the loss due to the ion jump mechanism. However, for the specimens with $\phi = 0.28$, the hump is not pronounced and only a power law type of increase in the ε'' value is observed (particularly for

the PC specimen, where the number of pores is lower). This is because the conduction losses dominate in the very low frequency region as compared to the ion jump losses, because of the lower porosity level relating to the more compact structure, which allows more conduction. Interestingly, as mentioned earlier, the f_p value is 8 kHz for the PC specimen and 1 kHz for the PF specimen. Now f_p can be expressed [8] in terms of the activation energy (W) and temperature (T) in the following way:

$$f_p = \nu \exp\left(-\frac{W}{kT}\right)$$

where k is the Boltzmann constant. If W_{PC} and W_{PF} represent the activation energies in the case of PC and PF specimens and f_{pPC} and f_{pPF} represent the corresponding hump frequencies, then

$$W_{PC} - W_{PF} = -kT \ln\left(\frac{f_{pPC}}{f_{pPF}}\right).$$

Due to the interfacial polarization effect, charges build up at the pore boundary and hence the activation energy should depend on the pore characteristics. As the increase in the pore surface area increases the barrier height and at the same time the increase in the volume increases the probability of hopping and migration, the ratio of the activation energies for PC and PF specimens can be approximated as the ratio of the corresponding specific surface areas (κ, the ratio of pore surface to volume), i.e., $\frac{W_{PC}}{W_{PF}} = \frac{\kappa_{PC}}{\kappa_{PF}}$.

From the above comparison, the values of W_{PC} and W_{PF} are estimated to be 103.9 and 157.7 meV respectively.

At high enough frequencies, the building up of the charges occurs only locally within grains, because charge build-up for higher length scales cannot follow the field and hence porosity does not affect ε' much at high frequencies. The reason for the fourth observation is not clear, but the difference in interconnectivity of the pores or grains between the two cases may be one possible factor. As the soaking time of the specimens with $\phi = 0.39$ is negligible compared to that for the specimens with $\phi = 0.28$, the interconnectivity of the pores is greater for the former.

It is seen from table 3 that the value of the parameter m, the exponent parameter for the frequency power law for ε' (in the case of $\phi = 0.28$), is $\sim$1.2 times greater for the PC specimen than for the PF specimen. Similarly, in the case of $\phi = 0.39$, the value of the parameter m is $\sim$1.6 times greater for the PC specimen than for the PF specimen. Strikingly, the ratio of the specific surface area (κ) of the PF specimen to that of the PC specimen in the case of $\phi = 0.28$ is $\sim$1.3 and that in the case of $\phi = 0.39$ is 1.5. This implies that the ratio of the m value for the PC specimen to that for the PF one is nearly identical to the ratio of the specific surface area of the PF specimen to that of the PC one, which implies the possibility that m varies inversely to the specific pore surface area.

5. Conclusions

In summary, the present investigation shows that the low frequency dielectric response of porous yttria-stabilized zirconia ceramic for significant pore volume fraction depends not only on the porosity but also on the other pore characteristics such as the pore size distribution, specific surface area, pore morphology. This is primarily due to the interfacial polarization effects, ion conduction and hopping. The hump in the ε'' spectrum for the specimens with $\phi = 0.39$ appears because of the loss due to the ion jump mechanism. The hump is absent for the specimens with $\phi = 0.28$ because the conduction losses dominate over the ion jump losses at very low frequencies. This is so because the lower porosity level related to the more

compact structure in specimens with $\phi = 0.28$ helps to produce more ion migration. From the comparison of the SANS results and dielectric results, the activation energies for the PC and PF specimens with $\phi = 0.39$ were found to be 103.9 and 157.7 meV respectively. The exponent m, in the frequency power law for ε', has been found to be inversely proportional to the specific surface area of the pores. A detailed theoretical model able to explain such variation of the frequency dependent dielectric response with pore characteristics is desirable.

Acknowledgments

We would like to thank Dr P U Sastry of the Solid State Physics Division, Bhabha Atomic Research Centre, for his kind help in the dielectric measurements.

References

[1] Kingery W, Bowen H K and Uhlmann D R 1976 *Introduction to Ceramics* 2nd edn (New York: Wiley) chapter 20, p 686
[2] Gurevisch V L and Tagantsev A K 1991 *Adv. Phys.* **40** 719–67
[3] Penn S J, Alford N M, Templeton A, Wang X, Xu M, Reece M and Schrapel K 1997 *J. Am. Ceram. Soc.* **80** 1885–8
[4] Valant M and Suvorov D 2003 *Mater. Chem. Phys.* **79** 104–10
[5] Alford N M and Penn S J 1996 *J. Appl. Phys.* **80** 5895–8
[6] Ibarra A, Heidinger R and Molla J 1992 *J. Nucl. Mater.* **191–194** 530
[7] Iddles D M, Bell A J and Moulson A J 1992 *J. Mater. Sci.* **27** 6303
[8] Jonscher A K 1983 *Dielectric Relaxation in Solids* (London: Chelsea Dielectrics Press)
[9] van Beek L K H 1967 *Progress in Dielectrics* vol 7, ed J B Birks (London: Heywood Books) p 69
[10] Kuang W and Nelson S O 1997 *J. Colloid Interface Sci.* **193** 242
[11] Tuncer E 2004 *J. Phys. D: Appl. Phys.* **37** 334–42
[12] Sen D, Patra A K, Mazumder S and Ramanathan S 2002 *J. Alloys Compounds* **340** 236–41
[13] Sen D, Patra A K, Mazumder S and Ramanathan S 2003 *J. Alloys Compounds* **361** 270–5
[14] Sen D, Mahata T, Patra A K, Mazumder S and Sharma B P 2003 *J. Alloys Compounds* **364** 304–10
[15] Sen D, Mazumder S and Tarafdar S 2002 *J. Mater. Sci.* **37** 941–7
[16] Strunz P, Schumacher G, Vassen R and Weidenmann A 2004 *Acta Mater.* **52** 3305–12
[17] Allen A J, Ilavsky J, Long G G, Walace J S, Berndt C C and Herman H 2001 *Acta Mater.* **49** 1661–75
[18] Ilavsky J, Long G G, Allen A J and Berndt C C 1999 *Mater. Sci. Eng.* A **272** 215–21
[19] Betz U, Sturm A, Loeffler J F, Wagner W, Wiedenmann A and Hahn H 1999 *Nanostruct. Mater.* **12** 689–92
[20] Mazumder S, Sen D, Saravanan T and Vijayaraghavan P R 2001 *J. Neutron Res.* **9** 39–57
[21] Mazumder S, Jayaswal B and Sequeira A 1998 *Physica* B **241–243** 1222–4
[22] Mazumder S and Sequeira A 1989 *Phys. Rev.* B **39** 6370
[23] Mazumder S and Sequeira A 1990 *Phys. Rev.* B **41** 6272
[24] Lake J A 1967 *J. Appl. Crystallogr.* **23** 191
[25] Sneddon I N 1972 *The Use of Integral Transforms* (New York: McGraw-Hill) pp 298–352
Sneddon I N 1951 *Fourier Transform* (New York: McGraw-Hill) pp 48–70
[26] Watson G N 1922 *The Theory of Bessel Functions* (Cambridge: Cambridge University Press) pp 453–68
Watson G N 1944 *A Treatise on the Theory of Bessel Functions* 2nd edn (Cambridge: Cambridge University Press)
[27] Maxwell J C 1954 *A Treatise on Electricity and Magnetism* vol 1 (New York: Dover)
[28] Wagner W 1914 *Arch. Elektrotech.* **2** 371
[29] Niklasson G A 1987 *J. Appl. Phys.* **62** R1–14